# Dipolar order mapping based on spin-lock magnetic resonance imaging

Zijian Gao<sup>1</sup>, Qianxue Shan<sup>1</sup>, Ziqin Zhou<sup>1,2</sup>, Ziqiang Yu<sup>1</sup>, Weitian Chen<sup>1,\*</sup>

1.Department of Imaging and Interventional Radiology, Faculty of Medicine, The Chinese University of Hong Kong, Hong Kong.

2.MR Research Collaboration, Siemens Heathineers Ltd., Hong Kong.

\*Corresponding author:

Weitian Chen

Department of Imaging & Interventional Radiology

The Chinese University of Hong Kong

Shatin, Hong Kong, SAR

(852)-3505-1036

Email: wtchen@cuhk.edu.hk

**Abstract** 

**Purpose** 

Inhomogeneous magnetization transfer (ihMT) effect reflects dipolar order with a dipolar

relaxation time  $(T_{1D})$ , specific to motion-restricted macromolecules. We aim to quantify  $T_{1D}$ 

using spin-lock MRI implemented with a novel rotary-echo sequence.

Methods

In proposed method, we defined a relaxation rate  $R_{dosl}$  that is specific to dipolar order and

obtained as the difference of dual-frequency  $R_{1\rho}^{dual}$  relaxation and single-frequency  $R_{1\rho}^{single}$ 

relaxation. A novel rotary-echo spin-lock sequence was developed to enable dual-frequency

acquisition. We derive the framework to estimate  $T_{1D}$  from  $R_{dosl}$  under macromolecular

pool fraction (MPF) map constraints. The proposed approach was validated via Bloch-

McConnell-Provotorov simulation, phantom studies, and in-vivo white matter studies on a 3T

scanner.

Results

Simulations demonstrated that  $R_{dosl}$  exhibits an approximately linear relationship with  $T_{1D}$ .

Phantom experiments showed robust ihMT contrast in  $R_{dosl}$  and confirmed the feasibility and

reliability of  $T_{1D}$  quantification via  $R_{dosl}$ . In vivo white-matter studies further supported the

clinical potential of this  $T_{1D}$  mapping approach.

Conclusion

We propose a novel, clinical feasible method for  $T_{1D}$  quantification based on spin-lock MRI.

This method requires substantially fewer contrast-prepared images compared to the

conventional  $T_{1D}$  quantification approach. This technique provides a promising pathway for

robust MPF and  $T_{1D}$  quantification in a single rapid scan with reduced confounds.

Keywords: Dipolar order, Inhomogeneous magnetization transfer, Spin-lock

## 1.Introduction

In ordered tissues containing motion-restricted macromolecules, residual dipolar coupling (RDC) of motion-restricted protons is prominent and generate dipolar order. This manifests in magnetization transfer (MT) as an asymmetric MT spectrum after single-frequency saturation that re-symmetrizes under dual-frequency saturation. This phenomenon, known as the inhomogeneous magnetization transfer (ihMT) effect, reflects dipolar order and is specific to motion-restricted macromolecular such as myelin<sup>1,2</sup>. Therefore, the quantification of dipolar order in ihMT is significant: it indexes microscopic motion restriction in macromolecules and may capture mechanisms of tissue microstructure change.

To extend the MT model, Provotorov theory, as formulated by Goldman<sup>3</sup>, indicates that the MT pool can be subdivided into Zeeman reservoir and dipolar reservoir. The dipolar reservoir is characterized by dipolar order ( $\beta$ ) with the dipolar relaxation time  $T_{1D}$ . Varma et. al introduced ihMTR for in-vivo experiments to indicate the ihMT effect via a subtraction experiment between images acquired with single frequency saturation and dual frequency saturation<sup>4</sup>. They further proposed  $T_{1D}$  quantification using multiple ihMTR-weighted images with varied frequency-switching times during dual-frequency saturation<sup>5</sup>. However, this approach has high scan-time demands because it requires a sufficient number of ihMTR-weighted images (e.g. eight ihMTR datasets with different switch times<sup>5</sup>). Girard et. al defined the pseudo-quantitative ihMT (qihMT), reducing acquisitions, enhancing the SNR, and enabling wider use in human studies.<sup>6-9</sup>. Although qihMT shows promise for clinical applications, it may be confounded by water-pool contributions (e.g.  $T_1$  effect)<sup>10,11</sup>, and it remains semi-quantitative without directly quantifying dipolar order. In addition, the use of a fixed population for the MT pool (e.g., a fixed macromolecular proton fraction (MPF)) may introduce confounding effects<sup>5,9,11</sup>. Despite these limitations, pursuing  $T_{1D}$  quantification with minimized confounds and clinically feasible scan time remains highly valuable.

Recently, an off-resonance spin-lock based quantitative MT approach (MPF-SL) has been proposed that mitigates water-pool contributions, suppresses RDC effects from motion-restricted water molecule and enables rapid measurement of MPF, offering strong potential for

clinical application<sup>12–15</sup>. In MPF-SL, with appropriate off-resonance spin-lock parameters, the MT-specific relaxation rate  $R_{mpfsl}$  is derived from the difference in rotating-frame relaxation rates  $R_{1\rho}$ . This method demonstrates the advantage and clinical feasibility of spin-lock based quantitative MT approach. In this study, we further extend this approach to rapidly quantify dipolar relaxation time  $T_{1D}$  in addition to MPF in a single scan. We introduce a specific relaxation rate  $R_{dosl}$  that is highly sensitive to  $T_{1D}$  without water pool contribution. We implement dual-frequency spin-lock saturation using a novel rotary-echo spin-lock radiofrequency (RF) pulse cluster with variable switch times between positive and negative RF pulses.  $R_{dosl}$  is derived from the difference between  $R_{1\rho}$  measurements under dual-frequency and single-frequency spin-lock saturation.  $T_{1D}$  can be computed directly from  $R_{dosl}$ , with MPF-derived constraints improving accuracy.

This technique provides a novel and efficient method for  $T_{1D}$  quantification without dependence on water-pool parameters, requiring substantially fewer contrast-prepared images compared to the conventional  $T_{1D}$  quantification approach, and thus supporting robust and clinically feasible  $T_{1D}$  measurement. We demonstrate the method through simulations, phantom studies, and in vivo experiments.

## 2.Theory

In two-pool model for MT, tissue magnetization is commonly divided into the water pool  $(M_x^a, M_y^a, M_z^a)$  and the MT pool  $(M_z^b)$ . Accounting for residual dipolar couplings in motion-restricted macromolecules, and following Provotorov theory as formulated by Goldman<sup>3</sup>, the MT pool is further to indicate the Zeeman reservoir and the dipolar reservoir. The dipolar reservoir is characterized by dipolar order  $(\beta)$  with the dipolar relaxation time  $T_{1D}$ . The two-pool model is extended using the Bloch-McConnell-Provotorov equations with the magnetization vector<sup>2,16</sup>

$$\vec{M} = (M_{ax}, M_{ay}, M_{az}, M_{bz}, \beta)^T , \qquad (1)$$

which follows:

$$\frac{d}{dt}\vec{M} = A \cdot \vec{M} + \vec{C} . \tag{2}$$

A is a 5 x 5 system matrix:

$$A = \begin{pmatrix} -R_{2a} & -\Delta\omega & 0 & 0 & 0 \\ +\Delta\omega & -R_{2a} & +\omega_1 & 0 & 0 \\ 0 & -\omega_1 & -R_{1a} - k_{ab} & k_{ba} & 0 \\ 0 & 0 & k_{ab} & -R_{1b} - R_{rfb} - k_{ba} & R_{rfb}(\frac{\Delta\omega}{D}) \\ 0 & 0 & 0 & R_{rfb}(\frac{\Delta\omega}{D}) & -(\frac{1}{T_{1D}} + R_{rfb}(\frac{\Delta\omega}{D})^2) \end{pmatrix}$$
(3)

and  $\vec{C}$  is a constant vector representing the equilibrium magnetizations:

$$\vec{C} = (0,0, R_{1a}M_{0a}, R_{1b}M_{0b}, 0)^{\mathrm{T}}$$
(4)

where the  $R_{2a}$  and  $R_{1a}$  are the transverse and longitudinal relaxation rates for water pool, respectively.  $R_{1b}$  is the longitudinal relaxation rate for the MT pool.  $R_{rfb} = \omega_1^2 \pi g(T_{2b}, \Delta \omega)$  denotes the saturation rate, computed using a super-Lorentzian lineshape  $g(T_{2b}, \Delta \omega)$ .  $T_{2b}$  is the transverse relaxation time for the MT pool.  $M_{0a}$  and  $M_{0b}$  denote the equilibrium magnetizations of the water and MT pools, respectively.  $\Delta \omega$  is the resonance frequency offset (FO) and  $\omega_1$  is the frequency of spin-lock (FSL).  $k_{ab}$  and  $k_{ba}$  are the exchange rates between water pool and MT pool. D is associated with the local dipolar field<sup>3</sup>, which approximately equals to  $\frac{1}{T_{2b}\sqrt{15}}$ .

Notably, when dual-frequency radiofrequency (RF) is applied with simultaneous irradiation at positive and negative frequency, the saturation term proportional to  $(\frac{\Delta\omega}{D})$  cancels in Eq.3. Under the dual-frequency RF irradiation,

$$R_{rfb}\left(\frac{\Delta\omega}{D}\right) + R_{rfb}\left(\frac{-\Delta\omega}{D}\right) = 0. \tag{5}$$

It indicates the contribution from dipolar reservoir can be removed using dual-frequency RF irradiation. The reduced  $A_{dual}$  is further driven by:

$$A_{dual} = \begin{pmatrix} -R_{2a} & -\Delta\omega & 0 & 0\\ +\Delta\omega & -R_{2a} & +\omega_1 & 0\\ 0 & -\omega_1 & -R_{1a} - k_{ab} & +k_{ba}\\ 0 & 0 & +k_{ab} & -R_{1b} - R_{rfb} - k_{ba} \end{pmatrix}$$
(6)

In the rotating frame,  $R_{1\rho}$  is primarily governed by the least negative eigenvalue of A and  $A_{dual}$ :

$$R_{1\rho}^{single} = R_w(\Delta\omega, \omega_1) + R_{mt}^d(\Delta\omega, \omega_1)$$
 (7)

and

$$R_{10}^{dual} = R_w(\Delta\omega, \omega_1) + R_{mt}^{nd}(\Delta\omega, \omega_1)$$
 (8)

 $R_w$  is the effective relaxation rate of the water pool.  $R_{mt}^d$  is the relaxation rate associated with MT pool with dipolar order effect, whereas  $R_{mt}^{nd}$  denotes the relaxation rate without dipolar order effect.

With single frequency and dual frequency spin-lock RF irradiation, the specific relaxation rate  $R_{dosl}$  can be approximately obtained as the difference between  $R_{1\rho}^{single}$  and  $R_{1\rho}^{dual}$ :

$$R_{dosl} = R_{1\rho}^{dual} - R_{1\rho}^{single} = R_{mt}^{nd} - R_{mt}^{d}$$

$$= \frac{k_{ba}^{2} f_{b} (f_{b} + 1) R_{rfb} (R_{rfb} + R_{1b}) T_{1D} (\frac{\Delta \omega}{D})^{2}}{[k_{ba} (f_{b} + 1) + R_{rfb} + R_{1b}] [(k_{ba} (f_{b} + 1) + R_{1b}) (1 + R_{rfb} (\frac{\Delta \omega}{D})^{2} T_{1D}) + R_{rfb}]}$$
(9)

The relaxation rate  $R_{dosl}$  is associated with the dipolar order parameter  $T_{1D}$ . Here,  $f_b$  is the pool population ratio of MT pool, and MPF =  $f_b/(f_b+1)$  .  $T_{1D}$  can be determined when MPF has been pre-quantified to provide a constraint. Note the parameters  $k_{ba}$ ,  $R_{1b}$  and  $T_{2b}$  are often treated as constants in human studies<sup>17</sup>.

Both  $R_{1\rho}^{single}$  and  $R_{1\rho}^{dual}$  are measured with the same  $\Delta\omega$  and  $\omega_1$  under the condition  $\Delta\omega\gg\omega_1$ , using single-frequency and dual-frequency spin-lock RF pulses, respectively. Under these matched conditions, the contribution of  $R_w(\Delta\omega,\omega_1)$  can be removed in subtraction. The details of the derivation of Eq. 9 are provided in Appendix.

## 3.Method

#### 3.1 Acquisition scheme

At the saturation pulse based ihMT acquisition scheme, dual-frequency saturation is applied using rapid alternation at positive and negative frequency on a minimal timescale<sup>5</sup>. Similarly, we proposed a modified rotary echo spin-lock RF pulse cluster with positive/negative rotary

pulse alternating with a switch time  $T_s$ . By the  $T_{1D}$  filtering effect<sup>18,19</sup>, dual-frequency spin-lock is achieved when  $T_s$  is shorter than the tissue  $T_{1D}$  (Figure 1, lower panel). In contrast, single frequency spin-lock is implemented with a long  $T_s$  that considerably exceeds the tissue  $T_{1D}$  (Figure 1, upper panel). This modified rotary-echo spin-lock RF pulse cluster provides a practical method to acquire  $R_{1D}^{single}$  and  $R_{1D}^{dual}$ .

For in vivo experiment, directly measuring of  $R_{1\rho}^{single}$  and  $R_{1\rho}^{dual}$  and then computing their difference to obtain  $R_{dosl}$  can be challenging. It requires multiple spin-lock prepared images with sufficiently long spin-lock time for robust quantification which is constrained by SAR and hardware limitations. Following the approach reported in  $^{12,14}$ , we can collect data and calculate the difference of  $R_{1\rho}^{single}$  and  $R_{1\rho}^{dual}$  directly instead of measuring them individually, which enables fast and robust measurement of  $R_{dosl}$ . Specifically, four spin-lock-prepared images are acquired:  $M_{notog}^{(1)}, M_{notog}^{(2)}, M_{tog}^{(2)}$ , and  $M_{tog}^{(2)}$ .  $R_{dosl}$  is then obtained as

$$R_{\text{dosl}} = R_{1\rho}^{dual} - R_{1\rho}^{single} = -\log\left(\frac{M_{tog}^{(2)} - M_{notog}^{(2)}}{M_{tog}^{(1)} - M_{notog}^{(1)}}\right) / TSL$$
 (10)

Here,  $M_{notog}^{(1)}$  is a single-frequency spin-lock weighted image associated with  $R_{1\rho}^{single}$ , acquired with long  $T_s$ , whereas  $M_{notog}^{(2)}$  is a dual-frequency spin-lock weighted image related to  $R_{1\rho}^{dual}$ , acquired with short  $T_s$ .  $M_{notog}^{(1)}$  and  $M_{notog}^{(2)}$  are acquired a the same  $\Delta \omega$  and  $\omega_1$ . Similarly,  $M_{tog}^{(1)}$  and  $M_{tog}^{(2)}$  are collected using the same parameters as  $M_{notog}^{(1)}$  and  $M_{notog}^{(2)}$ , respectively, but with the manipulation of the initial magnetization (i.e. applying a 180-degree inversion pulse before spin-lock RF pulses).

To quantify  $T_{1D}$  from  $R_{dosl}$ , we further estimate MPF using the MPF-SL method<sup>12</sup>.

As shown in the acquisition workflow in Figure 2, totally six off-resonance spin-lock prepared acquisitions are required to calculate MPF and  $T_{1D}$ .  $R_{dosl}$  is computed from the pairs  $M_{tog}^{(1)}/M_{notog}^{(1)}$  and  $M_{tog}^{(2)}/M_{notog}^{(2)}$  using  $\Delta R_{1\rho}$  calculator based on Eq.10.  $R_{mpfsl}$  is derived from  $M_{tog}^{(2)}/M_{notog}^{(2)}$  and  $M_{tog}^{(3)}/M_{notog}^{(3)}$  under the same calculation framework,

and then converted to MPF via a dictionary-based approach<sup>20</sup>.

Subsequently,  $T_{1D}$  map is estimated from  $R_{dosl}$  using  $T_{1D}$  solver, with MPF map providing constraints. This solver can employ non-linear least-squares fitting with:

$$T_{1D} = \operatorname{argmin}(R_{dosl}^{acq}(\Delta\omega, \omega_1, MPF) - R_{dosl}^{theor}(\Delta\omega, \omega_1, MPF))$$
(11)

 $R_{dosl}^{theor}$  is theorical  $R_{dosl}$  based on Eq.9 and  $R_{dosl}^{acq}$  is acquired  $R_{dosl}$  obtained by MRI acquisition. Alternatively, a dictionary-based solver can be used. For the dictionary approach, an  $R_{dosl}$  dictionary is generated over MPF = 0-20%,  $B_1 = 0.8$ -1.3 n.u., and  $T_{1D} = 0$ -15 ms.  $T_{1D}$  is then estimated by selecting the dictionary entry whose  $R_{dosl}$  best matches the measured value, using the acquired  $B_1$  and MPF as constraints.

#### 3.2 Simulation studies

## 3.2.1 Simulation study 1: Accuracy of approximate $R_{dosl}$ and its relationship to $T_{1D}$

The analytical expression of  $R_{dosl}$  in equation 9 is based on certain approximations. To assess the accuracy of this analytical expression of  $R_{dosl}$ , we compared it against the numerically solved  $R_{dosl}$  obtained by integrating the Bloch-McConnell-Provotorov equation using custom MATLAB code. In this comparison, we used the MT parameters of white matter taken from previous publications<sup>21,22</sup>:  $T_{1a} = 1840ms$ ,  $T_{1b} = 340ms$ ,  $T_{2a} = 69ms$ ,  $T_{2b} = 10\mu s$ ,  $f_{b} = 13.9\%$ , and  $k_{ba} = 23s^{-1}$ . We evaluated  $T_{1D}$  of 1, 3, 5, 7, and 10ms, based on previously study reported range of  $T_{1D}$  in white matter<sup>5,19</sup>. The range of FSL and FO, across common experimental range, were set to 100-800Hz and 2-12kHz, respectively.

Furthermore, we analyzed the relationship between  $R_{dosl}$  and  $T_{1D}$  to theoretically validate the sensitivity of  $R_{dosl}$  to  $T_{1D}$ .

## 3.2.2 Simulation study 2: Selection of acquisition parameters and discrepancy of estimated $T_{1D}$

In our acquisition workflow, the  $T_{1D}$  map is estimated from the  $R_{dosl}$  map, with MPF map providing constraints to the  $T_{1D}$  solver. We opted for a fitting-based approach, which offers greater precision, flexibility, and extensibility compared with dictionary-based methods. When using the fitting approach, however, the minor discrepancy between the acquired  $R_{dosl}$ , collected using single and dual frequency spin-lock sequence in Eq.10, and the approximate  $R_{dosl}$  in Eq.9 can propagate and lead to bias in the fitted  $T_{1D}$ . Such bias between acquired  $R_{dosl}$  and approximate  $R_{dosl}$  can be minimized by optimizing acquisition parameters.

To identify effective acquisition parameters, we compared the acquired  $R_{dosl}$  and approximate  $R_{dosl}$ , and computed the bias in fitted  $T_{1D}$  from acquired  $R_{dosl}$  using the Levenberg-Marquardt algorithm. We performed numerical simulations to compute the acquired  $R_{dosl}$  by modeling single and dual frequency spin-lock sequence and solving the Bloch-McConnell-Provotorov equations in MATLAB with the ode45 solver.  $T_{1D}$  was set to 6.2 ms and the remaining white matter parameters were identical to those in Simulation Study 1. The  $T_s$  of dual and single frequency spin-lock pulse are chosen 0.5 ms and 40 ms, respectively, given that white matter  $T_{1D}$  typically ranges from 3 to 10 ms<sup>11</sup>. FSL values ranged from 100 to 1000 Hz, FO from 2 to 12 kHz, and TSL from 20 to 100 ms.

After selecting the acquisition parameters, we compared  $T_{1D}$  estimates obtained with the fitting-based approach versus the dictionary-based approach. Simulated MRI signals were corrupted with additive white Gaussian noise at SNRs of 50, 80 and 100, respectively.

#### 3.3 Phantom studies

#### 3.3.1 Preparation of phantoms and experimental setup.

Agar phantoms and Prolipid 161 (PL161; Ashland Specialty Ingredients, USA) phantoms were prepared for this study and underwent the same MRI protocol. Four phantoms were made with 1%,

2%, 3% and 4% concentration, respectively. Four PL161 phantoms were made with PL161 mixed with pure water H<sub>2</sub>O with 4%, 8%, 12% and 16% weight per weight ratio concentration, respectively. PL161 exhibits strong ihMT contrast and was therefore regarded as a validation of the ihMT effect.

MRI data acquisitions were performed using a 3T Prisma scanner (Siemens Healthineers, Germany) equipped with a 64-channel head-neck receiver coil at the room temperature (~20°C). 2D MPF-SL and  $R_{dosl}$  measurements were performed with the parameters as follows: field of view (FOV) of 240 mm×240mm, voxel size of 2×2×5 mm³, and one slice. The sequence parameter related to  $R_{dosl}$  measurement were  $\Delta\omega^{(1)} = \Delta\omega^{(2)} = 2\pi \cdot 5000 \, rad/s$ ,  $\omega_1^{(1)} = \omega_1^{(2)} = 2\pi \cdot 5000 \, rad/s$ ,  $\omega_1^{(1)} = \omega_1^{(2)} = 2\pi \cdot 5000 \, rad/s$ ,  $\omega_1^{(1)} = \omega_1^{(2)} = 2\pi \cdot 5000 \, rad/s$ ,  $\omega_1^{(1)} = \omega_1^{(2)} = 2\pi \cdot 5000 \, rad/s$ ,  $\omega_1^{(1)} = \omega_1^{(2)} = 2\pi \cdot 5000 \, rad/s$ ,  $\omega_1^{(1)} = \omega_1^{(2)} = 2\pi \cdot 5000 \, rad/s$ ,  $\omega_1^{(1)} = \omega_1^{(2)} = 2\pi \cdot 5000 \, rad/s$ ,  $\omega_1^{(1)} = \omega_1^{(2)} = 2\pi \cdot 5000 \, rad/s$ ,  $\omega_1^{(2)} = 2\pi \cdot$ 

#### 3.3.2 Data analysis

To convert the  $R_{dosl}$  to  $T_{1D}$ , we used commonly used assumptions that the MT parameters  $T_{1b}$ ,  $T_{2b}$  and  $k_{ba}$  are constant. For agar phantoms, we used  $T_{1b} = 1000 \, ms$ ,  $T_{2b} = 10 \, \mu s$  and  $k_{ba} = 230 \, s^{-1}$ . For PL161 phantoms, we used  $T_{1b} = 220 \, ms$ ,  $T_{2b} = 17 \, \mu s$  and  $k_{ba} = 46 \, s^{-1}$ , respectively<sup>23,24</sup>. Both fitting-based  $T_{1D}$  solver with Levenberg-Marquardt algorithm and dictionary-based  $T_{1D}$  solver with resolution of 0.01ms of  $T_{1D}$  were applied. MPF maps were derived from  $R_{mpfsl}$  and used as priors for  $T_{1D}$  estimation.

Test-retest agreement for PL161 was assessed using Bland-Altman analysis and intraclass correlation coefficients (ICC).

#### 3.4 In-vivo studies

#### 3.4.1 Experiment setup

The study was performed in accordance with the institutional ethical guidelines and the ethical standards of the 1964 Declaration of Helsinki and its subsequent amendments. Ten healthy

volunteers (age range 25-30 years; 5 male and 5 female) were enrolled in this study under the approval of our Institutional Review Board (Ref No. 2016.150). Exclusion criteria included a history of neurological diseases, brain injury, major psychiatric illness, or drug or alcohol misuse. Written informed consent was obtained from all participants.

All MRI scans were performed in a 3T Prisma scanner, with the same equipment and temperature conditions as in the phantom studies. Each volunteer underwent test-retest MRI examinations with a 7-10 day interval.

#### 3.4.2 MRI protocol

The MRI scan protocol included the following parameters with the identical FOV of 260 mm×260 mm:

- (1) A 3D  $T_1$ -weighted axial image was acquired for anatomical imaging using magnetization prepared rapid gradient echo (MP-RAGE) sequence with the following parameters: TE = 1.67 ms, TR = 1900 ms, voxel size =  $1.5 \times 1.5 \times 2.5$  mm<sup>3</sup>, and a scan time of 2 minutes, 3 seconds.
- (2) B1 and B0 field maps were obtained using the Siemens clinical brain protocol. For B1 mapping, the voxel size was  $2.9 \times 2.9 \times 2.5$  mm³ with a 57 s acquisition. For B0 mapping, the voxel size was  $1.5 \times 1.5 \times 5$  mm³ with a 6 s acquisition time.
- (3) A DTI scan was performed with TE = 77 ms, TR = 3200 ms, voxel size =  $2.5 \times 2.5 \times 2.5 \times 2.5 \text{ mm}^3$ , b-value =  $0 \text{ s/mm}^2$  and  $1000 \text{ s/mm}^2$ , 30 diffusion directions, and a scan time of 3 minutes, 58 seconds.
- (4) MPF and  $T_{1D}$  are acquired in a single scan. 2D  $R_{dosl}$  acquisitions were conducted with  $\Delta\omega^{(1)}=\Delta\omega^{(2)}=2\pi\cdot 5000~rad/s$ ,  $\omega_1^{(1)}=\omega_1^{(2)}=2\pi\cdot 500~rad/s$ ,  $T_s^{(1)}=40ms$ ,  $T_s^{(2)}=0.5~ms$ , TSL=80ms. The parameters related to MPF calculations are as follows:  $\omega_1^{(3)}=2\pi\cdot 100~rad/s$ ,  $\Delta\omega^{(3)}=2\pi\cdot 1000~rad/s$ ,  $N=\Delta\omega^{(2)}/\Delta\omega^{(3)}=\omega_1^{(2)}/\omega_1^{(3)}=5$ ,  $T_s^{(2)}=T_s^{(3)}=0.5ms$ , TSL=80ms. The voxel size was  $1.5\times 1.5\times 5~mm^3$ , the number of slices was 3, and the acquisition time was 2 min 3s per slice.

In addition, one volunteer underwent Z-spectroscopic data acquisition using an MT-weighted spoiled gradient echo (GRE) sequence with a Gaussian pulse for off-resonance saturation with 11  $\Delta$  values (2, 3, 4, 6, 8, 12, 16, 20, 32, and 36 kHz) and an independence  $R_1$  maps acquisition to calculate the MT parameters.  $R_1$  maps were obtained using the  $B_1$  corrected variable flip angle

(VFA) method and an inline reconstruction with MapIt processing tool (Siemens Healthcare, Germany).

#### 3.4.3 Data processing and analysis

We used the qMRLab open-source tool (https://qmrlab.org/) to fit the Z-spectroscopic data and obtain MT parameters. Specifically, we estimated  $k_{ba} = 17s^{-1}$ ,  $T_{2b} = 9.7\mu s$  and set the  $T_{1b} = 340ms$  based on literature<sup>22</sup>. These parameters were then used for further processing.

The MPF maps were derived from  $R_{\rm mpfsl}$  and as a prior map for  $T_{1D}$  quantification. The processing of MPF maps using standard MPF method based on dictionary approach<sup>20</sup>.

 $R_{
m dosl}$  maps were calculated from four spin-lock prepared images (e.g.  $M_{tog}^{(1)}/M_{notog}^{(1)}$  and  $M_{tog}^{(2)}/M_{notog}^{(2)}$ ) via Eq.10.  $T_{1D}$  maps were then obtained from  $R_{
m dosl}$  with MPF constraints using both a fitting-based solver (Levenberg–Marquardt, MATLAB) and a dictionary-based solver (dictionary generated from the Bloch–McConnell–Provotorov equations). In addition,  $B_1$  maps were used for the correction of RF inhomogeneity.

To analyze  $T_{1D}$  maps in ROIs of white matter, the  $T_1$ -weighted images and DTI data were used for fiber bundles segmentation. The TractSeg opensource tool (https://github.com/MIC-DKFZ/TractSeg) was employed to segment the fiber bundles of white matter <sup>25</sup>. In this study, the acquired slices for MPF measurement primarily included 16 regions of white matter fiber bundles: Arcuate fascicle (AF left, AF right), Anterior Thalamic Radiation (ATR left, ATR right), Corpus Callosum Genu (CC 2), Corpus Callosum Rostral body (CC 3), Corpus Callosum Posterior midbody (CC 5), Corpus Callosum Splenium (CC 7), Cingulum (CG left, CG right), Optic radiation (OR left, OR right), Middle longitudinal fascicle (MLF left, MLF right), and Fronto-pontine tract (FPT left, FPT right).

To assess test-retest reproducibility, we performed Bland-Altman and correlation analyses. The Bland-Altman analysis quantified the mean difference (bias) and limits of agreement (LoA). Correlation was evaluated using the ICC from a two-way random-effects model. These test-

retest analyses were applied to  $R_{\rm dosl}$ ,  $T_{1D}$  maps derived from fitting-based  $T_{1D}$  solver  $(T_{1D}_{\rm -} {\rm fit})$ , and  $T_{1D}$  maps derived from dictionary-based  $T_{1D}$  solver  $(T_{1D}_{\rm -} {\rm dic})$  across 16 major white matter bundles. Before analysis, we performed outlier cleaning within each of the 16 bundles, retaining measurements within mean  $\pm$  1std.

## 4. Results

Figure 3 shows the comparison of approximate  $R_{dosl}$  and its numerical solution. The approximate results (markers) closely follow the numerical curves (solid lines) across both conditions. These observations indicate that the approximate  $R_{dosl}$  proposed in this study provides a reliable estimate across the tested parameter ranges, making it suitable for practical applications.

Figure 4 illustrates the sensitivity of  $R_{dosl}$  to  $T_{1D}$ . At a fixed FSL of 500 Hz and for selected FO values of 5, 6, and 7 kHz,  $R_{dosl}$  increases markedly as  $T_{1D}$  rises from 1 to 10 ms. The relationship between  $R_{dosl}$  and  $T_{1D}$  is approximately linear, highlighting the high sensitivity of  $R_{dosl}$  to  $T_{1D}$ .

Figure 5 presents the simulations comparing acquired and approximate  $R_{dost}$ , and reports the  $T_{1D}$  fitting error analysis. As shown in Figure 5 (a)-(c), the acquisition parameters of spin-lock pulses should be optimized to achieve reliable  $R_{dost}$  measurement, including FO, FSL, and TSL. Consider the results from Figure 5 (a), (d), and (g), the choice of FO is preferred to a range FO=4-7kHz under FSL=500Hz. The results in Figure (b), (e), and (h) indicate FSL = 500 Hz is preferred to lower FSL. TSL should be sufficiently long (e.g., 80 ms) to minimize relative error, as shown in Figure (c), (f), and (i). In this study we chose the FSL=500Hz, FO=5000Hz and TSL=80ms. All these choices are within SAR and RF hardware limit during in-vivo scan.

Figure 6 exhibits the distribution of  $T_{1D}$  estimation across different SNR levels using fitting-based  $T_{1D}$  solver and dictionary-based  $T_{1D}$  solver. The results demonstrate better

performance of fitting-based  $T_{1D}$  solver at low SNR (bias is -0.635 ms and -2.025 ms at SNR level of 50 for the fitting approach and the dictionary approach, respectively), and higher accuracy of dictionary-based  $T_{1D}$  solver at high SNR (bias is 0.345 ms and -0.080 ms at SNR level of 100 for the fitting approach and the dictionary approach, respectively).

Figure 7(a) shows the results of MPF-SL acquisitions for agar and PL161 phantoms. Figure 7(b) presents the  $R_{dosl}$  and  $T_{1D}$  map from both fitting-based and dictionary  $T_{1D}$  solver.  $R_{dosl}$  highlighted the contrast of PL161 phantom, demonstrating its sensitivity to ihMT effect. In result of  $T_{1D}$  maps, the long  $T_{1D}$  of PL161 phantom is confirmed by our method, while agar phantom exhibit notable MPF but negligible  $T_{1D}$ , consistent with their lack of dipolar order terms. Figure 7(c) shows the relationships between  $R_{dosl}/T_{1D}$  and phantom concentration. Both  $R_{dosl}$  and  $T_{1D}$  appear to increase with higher PL161 concentration, whereas no obvious trend is observed with agar concentration.

Figure 8 presents in-vivo results from one volunteer (V1). The  $T_1$  weighted anatomical image for the selected slice and the 16 major white matter bundles are shown in Figure 8(a) and (b).  $R_{dosl}$  maps, in Figure 8(d), indicated the highlighted white matter compared with the MPF map in Figure 8(c).  $T_{1D}$ -fit and  $T_{1D}$ -dic maps are calculated from  $R_{dosl}$  and MPF maps, they retain similar contrast with  $R_{dosl}$  maps, as shown in Figure 8(d) and (f). The mean and standard deviation of  $R_{dosl}$ ,  $T_{1D}$ -fit and  $T_{1D}$ -dic maps across 16 major white matter fiber bundles in 10 volunteers are represented in Table 1. The significant difference of the contrast in the  $T_{1D}$  map and the MPF map indict these two parameters may carry different molecular signatures of tissues. Results for other volunteers are provided in the Supplementary Material.

Figure 9 reports test–retest repeatability from PL161 phantom studies and in vivo experiments. The PL161 phantom shows very good repeatability:  $R_{dosl}$  has bias = 0.003 Hz, LoA = -0.040 to 0.046 Hz, and ICC = 0.985;  $T_{1D}$ \_fit map has bias = 0.338 ms, LoA = -5.811 to 5.135 ms, and ICC = 0.982;  $T_{1D}$ \_dic map has bias = 1.315 ms, LoA = -1.460 to 4.085 ms, and ICC = 0.994. In vivo experiments show good repeatability:  $R_{dosl}$  has bias = 0.003 Hz, LoA = -0.028 to 0.033 Hz, and ICC = 0.718;  $T_{1D}$ \_fit map has bias = 0.006 ms, LoA = -0.623 to 0.610 ms,

and ICC = 0.700;  $T_{1D}$ \_dic map has bias = 0.002 ms, LoA = -0.739 to 0.743 ms, and ICC = 0.704.

## 5.Discussion

## 5.1 Promise of $T_{1D}$ quantification based spin-lock

Unlike conventional MT, ihMT isolates dipolar order that is specific to motion-restricted macromolecules with long  $T_{1D}$  components, such as myelin.  $T_{1D}$  provides the specifical sensitivity to microstructural organization, whereas MT-derived parameters such as the MPF primarily reflect macromolecular content. Clinically, ihMT metrics have been shown to correlate with disability and outperform MT in multiple sclerosis (MS)<sup>26</sup>, to detect spinal cord damage with higher sensitivity<sup>27</sup>, and to track lesion recovery dynamics consistent with remyelination, including effects of lesion size and periventricular proximity<sup>28</sup>. However, these clinical studies only focus on ihMTR or pseudo-ihMTR rather than direct  $T_{1D}$  quantification, and the resulting measures may be influenced by contributions from the water pool (e.g. T1 effect)<sup>10,11</sup> and MT pool (e.g. MPF). Our proposed method offers a framework for  $T_{1D}$  quantification with simultaneous MPF estimation scan and minimizes water pool contributions. It enables rapid  $T_{1D}$  quantification with reduced confounding effects.

In addition, MPF and  $T_{1D}$  represent different molecules signature of tissue. Specifically, MPF primarily reflects the macromolecular content, while  $T_{1D}$  is sensitive to microstructural organization. Our proposed method enables simultaneous mapping of MPF and  $T_{1D}$  in a single fast scan, providing a more comprehensive characterization of tissue properties.

Beyond myelin, dipolar-order quantification may be translated to other tissues rich in motion-restricted macromolecules. Cartilage, with its dense collagen-proteoglycan matrix, exhibits ihMT effects<sup>29</sup> and may support  $T_{1D}$  quantification sensitive to matrix integrity and degeneration. Applying our proposed method in vivo to cartilage is a promising direction that

## 5.2 Potential Confounding factors for Spin-Lock–Based $T_{1D}$ quantification

Previous study presented the value of  $T_{1D}$  in white matter spanning different ranges, including ~2.8-6.6 ms<sup>5</sup> and ~10 ms<sup>30</sup>. In this study, we obtained the  $T_{1D}$  of white matter around 3.9-5.1 ms. Validating and interpreting the value of  $T_{1D}$  remains challenging. In our acquisition strategy, with  $T_s^{(1)}$ =40 ms and  $T_s^{(2)}$ =0.5 ms, the  $T_{1D}$  filtering effect enables sensitivity to components between roughly 0.5 and 40 ms. To probe the dominant  $T_{1D}$  components in white matter using our method, we performed additional in-vivo experiments varying  $T_s^{(2)}$  from 0.5 to 20 ms. As shown in Figure S1 at the Supplementary Material, the white matter is highlighted when  $T_s^{(2)}$  less than 10 ms, with further enhanced at  $T_s^{(2)}$  less than 1 ms. This suggests that the estimated  $T_{1D}$  reflects a mixture of long components and very short components (<1 ms), yielding an apparent value in the range of 3.9–5.1 ms.

To derive the  $T_{1D}$  map from  $R_{dosl}$ , we use MPF quantification as an additional constraint and treat the remaining MT-pool parameters in Eq. 9 as constants (i.e.,  $k_{ba}$ ,  $R_{1b}$ , and  $T_{2b}$ ). However,  $k_{ba}$  reflects the exchange rate between the water and MT pools and can be modulated by tissue microenvironmental factors<sup>31</sup>, potentially undermining this assumption in certain clinical contexts. In addition,  $R_{1b}$  and  $T_{2b}$  exhibit orientation dependence in myelin tissues<sup>32,33</sup>. Therefore, the validity and impact of these constant-parameter assumptions warrant further investigation in future studies.

The orientation dependence of  $T_{1D}$  has been demonstrated by Morris et al<sup>34</sup>. They conducted ex-vivo spinal cord experiments, and the results suggest orientation dependence of ihMTR and  $T_{1D}$ . In contrast, orientation-independent MT quantification has been explored for spin-lock-based approaches in cartilage and myelin <sup>13,15</sup>. Therefore, potential orientation dependence in

our spin-lock based  $T_{1D}$  quantification also warrants further investigation.

Looking ahead, other spin-lock-based quantitative MT techniques, including fast MPF-SL and pulsed spin-lock approaches, may be leveraged for dipolar-order quantification using rapid and robust acquisition strategies. By employing the fast MPF-SL approach<sup>35</sup>, scan time can be further reduced, making it feasible to achieve comprehensive coverage of the brain with both  $T_{1D}$  and MPF quantification within 5 minutes with 3D acquisition. The pulsed spin-lock approach<sup>14</sup> can mitigate limitations imposed by RF hardware. This is particularly beneficial for body imaging and for applications at lower field strengths, where RF power constraints are typically more pronounced. Integrating these methods with enhanced dictionaries and constrained fitting schemes represents a promising direction for translating  $T_{1D}$  mapping into routine clinical workflows.

## 5.3 Challenge and limitations

Although our theoretical analysis and experimental results support the reliability, clinical feasibility and repeatability of spin-lock based  $T_{1D}$  quantification, several limitations and challenges warrant further investigation: (1) A standardized benchmark for  $T_{1D}$  quantification is needed to rigorously validate the accuracy of  $T_{1D}$  maps produced by the proposed method. Saturation-pulse-based  $T_{1D}$  quantification can serve as a reference for comparative experiments in further studies. (2) The relationship between  $R_{dosl}$  and tissue microstructural mechanisms requires in-depth investigation. Validation can be pursued through ex vivo studies with histological analysis to directly compare with the proposed MRI technique. (3) The correlation between the proposed  $T_{1D}$  quantification and microstructure-related health states (e.g., demyelination and remyelination) remains to be demonstrated. Additional clinical studies are necessary to establish the utility of this approach in routine clinical practice.

## 6.Conclusion

We present a theory and methodology for quantifying dipolar order using an off-resonance spin-

lock MRI technique and demonstrate effective  $T_{1D}$  estimation with this approach. Compared with existing  $T_{1D}$  methods, our protocol requires only six spin-lock—weighted images and mitigates confounds from the water pool, enabling rapid and clinically feasible measurements. This approach can provide measurement of both MPF and  $T_{1D}$  in a single rapid scan and has the potential to accelerate the clinical adoption of molecular imaging based on magnetization transfer effect.

## Acknowledgment

This study was supported by a grant from the Research Grants Council of the Hong Kong SAR (Project GRF 14213322) and a grant from the Innovation and Technology Commission of the Hong Kong SAR (Project No. MRP/046/20x).

## Appendix

The  $R_{1\rho}^{single}$  is divided into  $R_w$  and  $R_{mt}^d$ . The effective water relaxation rate  $R_w$  is given by:

$$R_W = R_{1a}cos^2\varphi + R_{2a}sin^2\varphi \tag{A.1}$$

where  $cos^2 \varphi = \frac{\Delta \omega^2}{\omega_1^2 + \Delta \omega^2}$  and  $sin^2 \varphi = \frac{\omega_1^2}{\omega_1^2 + \Delta \omega^2}$ , and  $\varphi$  represents the direction of the spin-lock field.

To accurately approximate the effective  $R_{mt}^d$ , A in Eq. 3 can be shifted to  $A' = A - diag(R_w)^{-36}$ , which yields:

$$A' = \begin{pmatrix} -r_{2a} & -\Delta\omega & 0 & 0 & 0\\ +\Delta\omega & -r_{2a} & +\omega_1 & 0 & 0\\ 0 & -\omega_1 & -r_{1a} - k_{ab} & k_{ba} & 0\\ 0 & 0 & k_{ab} & -r_{1b} - k_{ba} & R_{rfb}(\frac{\Delta\omega}{D})\\ 0 & 0 & 0 & R_{rfb}(\frac{\Delta\omega}{D}) & r_d - \frac{1}{T_{1D}} \end{pmatrix}$$
(A.2)

Where  $r_{1a} = R_{1a} - R_w$ ,  $r_{2a} = R_{2a} - R_w$ ,  $r_{1b} = R_{1b} + R_{rfb} - R_w$ , and  $r_d = -R_{rfb} \left(\frac{\Delta \omega}{D}\right)^2 - \frac{1}{2} \left(\frac{\Delta \omega}{D$ 

 $R_w$ . Using Mathematica, the eigenvalue of the shifted system A' as follows:

$$R_{mt}^{d} = \frac{R_{rfb}^{2} T_{1D} \Delta \omega^{2} \cdot \mathcal{N}_{1} + D^{2} (1 - r_{d} T_{1D}) \cdot \mathcal{N}_{2}}{-R_{rfb}^{2} T_{1D} \Delta \omega^{2} \cdot \mathcal{G}_{1} + D^{2} \cdot \mathcal{G}_{2}}$$
(A.3)

$$\mathcal{N}_{1} = -(k_{ab} + r_{1a}) \left( \frac{r_{2a}^{2}}{\Delta \omega^{2}} + 1 \right) - r_{2a} \frac{\omega_{1}^{2}}{\Delta \omega^{2}}$$
(A.4)

$$\mathcal{N}_{2} = ((k_{ba}r_{1a} + (k_{ab} + r_{1a})r_{1b})\left(\frac{r_{2a}^{2}}{\Delta\omega^{2}} + 1\right) + (k_{ba} + r_{1b})r_{2a}\frac{\omega_{1}^{2}}{\Delta\omega^{2}})$$
(A.5)

$$G_1 = \frac{2r_{2a}((k_{ab} + r_{1a}))}{\Delta\omega^2} + \frac{r_{2a}^2}{\Delta\omega^2} + 1 + \frac{\omega_1^2}{\Delta\omega^2}$$
(A.6)

The term  $G_2$  can be further decomposed as:

$$G_2 = (G_{2a} + G_{2b} + G_{2c} + G_{2d} + G_{2e})$$
(A.7)

Each component is defined as follows:

$$\mathcal{G}_{2a} = \frac{2r_{1b}r_{2a}}{\Delta\omega^2}r_{1a} + (r_{1a} + r_{1b} + r_{1a}r_{1b}T_{1D})\frac{r_{2a}^2}{\Delta\omega^2}$$
(A.8)

$$\mathcal{G}_{2b} = -\frac{2r_{1b}r_{2a}r_dT_{1D}}{\Delta\omega^2}r_{1a} - (r_{1a}r_dT_{1D} + r_{1b}r_dT_{1D})\frac{r_{2a}^2}{\Delta\omega^2}$$
(A.9)

$$\mathcal{G}_{2c} = \frac{k_{ba}r_{2a}(2 + r_{2a}T_{1D} - 2r_dT_{1D})}{\Delta\omega^2} r_{1a} + k_{ab}(1 - r_dT_{1D} + T_{1D}) \frac{r_{2a}^2}{\Delta\omega^2} + 2r_{1b}(1 - r_dT_{1D}) \frac{k_{ab}r_{2a}}{\Delta\omega^2}$$
(A.10)

$$G_{2d} = r_{1a}(1 + k_{ba}T_{1D} + r_{1b}T_{1D} - r_{d}T_{1D}) + (r_{1b} + k_{ab} + k_{ba}\left(\frac{r_{2a}^2}{\Delta\omega^2} + 1\right))(1 - r_{d}T_{1D}) + k_{ab}T_{1b}T_{1D}$$
(A.11)

$$G_{2e} = (k_{ba} + r_{1b} + r_{2a} + (k_{ba} + r_{1b})r_{2a}T_{1D} - (k_{ba} + r_{1b} + r_{2a})r_{d}T_{1D})\frac{\omega_{1}^{2}}{\Delta\omega^{2}}$$
(A.12)

Considering our spin-lock pulse implementation and tissue parameters of water mater,

$$\Delta\omega/\omega_1\gg 1$$
 ,  $\Delta\omega\gg r_{2a}$ ,  $\Delta\omega\gg k_{ab}$  ,  $R_{1b}+R_{rfb}\gg R_{1a}$ , and  $R_{rfb}\left(\frac{\Delta\omega}{D}\right)^2\gg R_w$  are

satisfied. Subsequentially, we have  $R_W \cong R_{1a}$ ,  $r_{1a} \cong 0$ ,  $\omega_1^2/\Delta\omega^2 \cong 0$ ,  $r_{2a}^2/\Delta\omega^2 \cong 0$ ,  $k_{ab}r_{2a}/\Delta\omega^2 \cong 0$ ,  $r_{1b} \cong R_{1b} + R_{rfb}$ , and  $r_d \cong -R_{rfb} \left(\frac{\Delta\omega}{D}\right)^2$ . Substituting these into Eq. A.3-12, we obtained  $\mathcal{N}_1 \approx -k_{ab}$ ,  $\mathcal{N}_2 \approx k_{ab}r_{1b}$ ,  $\mathcal{G}_1 \approx 1$ , and the ignoration of  $\mathcal{G}_{2a}$ ,  $\mathcal{G}_{2b}$ ,  $\mathcal{G}_{2c}$ , and  $\mathcal{G}_{2e}$ .  $\mathcal{G}_{2d}$  can be simplified to

$$G_{2d} = (r_{1b} + k_{ab} + k_{ba})(1 + R_{rfb} \left(\frac{\Delta\omega}{D}\right)^2 T_{1D}) + k_{ab} r_{1b} T_{1D}$$
(A.13)

Approximate  $R_{mt}^d$  is further updated:

$$R_{mt}^{d} = \frac{-R_{rfb}^{2} T_{1D} \left(\frac{\Delta \omega}{D}\right)^{2} k_{ab} + \left(1 + R_{rfb} \left(\frac{\Delta \omega}{D}\right)^{2} T_{1D}\right) k_{ab} r_{1b}}{-R_{rfb}^{2} T_{1D} \left(\frac{\Delta \omega}{D}\right)^{2} + (r_{1b} + k_{ab} + k_{ba}) (1 + R_{rfb} \left(\frac{\Delta \omega}{D}\right)^{2} T_{1D}) + k_{ab} r_{1b} T_{1D}}$$

$$= \frac{k_{ab} (R_{rfb} + R_{1b}) + R_{rfb} \left(\frac{\Delta \omega}{D}\right)^{2} T_{1D} R_{1b}}{(k_{ab} + k_{ba}) \left(1 + R_{rfb} \left(\frac{\Delta \omega}{D}\right)^{2} T_{1D}\right) + (R_{rfb} + R_{1b}) (k_{ab} T_{1D} + 1) + R_{rfb} \left(\frac{\Delta \omega}{D}\right)^{2} T_{1D} R_{1b}}$$
(A.14)

It is notable that  $k_{ab}T_{1D}+1\cong 1$  and  $R_{rfb}\left(\frac{\Delta\omega}{D}\right)^2T_{1D}R_{1b}$  can be ignored due to its minimal value compared with other terms in numerator of Eq. A. 14. Therefore, the approximate  $R_{mt}^d$  is further given with  $k_{ab}=f_bk_{ba}$ :

$$R_{mt}^{d} \cong \frac{f_b k_{ba} (R_{rfb} + R_{1b})}{(k_{ba} (f_b + 1) + R_{1b}) \left(1 + R_{rfb} \left(\frac{\Delta \omega}{D}\right)^2 T_{1D}\right) + R_{rfb}}$$
(A.15)

Similarly,  $R_{mt}^{nd}$  from  $R_{1\rho}^{dual}$  can be derived by:

$$R_{mt}^{nd} \cong \frac{f_b k_{ba} (R_{rfb} + R_{1b})}{k_{ba} (f_b + 1) + R_{rfb} + R_{1b}}$$
(A.16)

Furthermore, we have the approximate  $R_{dosl}$ 

$$R_{dosl} = R_{1\rho}^{dual} - R_{1\rho}^{single} = R_{mt}^{nd} - R_{mt}^{d}$$

$$= \frac{k_{ba}^{2} f_{b}(f_{b}+1) R_{rfb}(R_{rfb}+R_{1b}) T_{1D}(\frac{\Delta \omega}{D})^{2}}{[k_{ba}(f_{b}+1) + R_{rfb} + R_{1b}][(k_{ba}(f_{b}+1) + R_{1b})(1 + R_{rfb}(\frac{\Delta \omega}{D})^{2} T_{1D}) + R_{rfb}]}$$
(A.17)

## Conflict of interest statement

Weitian Chen is a shareholder of Illuminatio Medical Technology Limited.

## Reference

- Girard OM, Prevost VH, Varma G, Cozzone PJ, Alsop DC, Duhamel G. Magnetization transfer from inhomogeneously broadened lines (ihMT): Experimental optimization of saturation parameters for human brain imaging at 1.5 Tesla. *Magn Reson Med*. 2015;73(6):2111-2121. doi:10.1002/mrm.25330
- Varma G, Girard OM, Prevost VH, Grant AK, Duhamel G, Alsop DC. Interpretation of magnetization transfer from inhomogeneously broadened lines (ihMT) in tissues as a dipolar order effect within motion restricted molecules. *J Magn Reson*. 2015;260:67-76. doi:10.1016/j.jmr.2015.08.024
- 3. M. Goldman. Spin Temperature and Nuclear Magnetic Resonance in Solids. Clarendon Press; 1970.
- Varma G, Duhamel G, de Bazelaire C, Alsop DC. Magnetization transfer from inhomogeneously broadened lines: A potential marker for myelin. *Magn Reson Med*. 2015;73(2):614-622. doi:10.1002/mrm.25174
- Varma G, Girard OM, Prevost VH, Grant AK, Duhamel G, Alsop DC. In vivo measurement of a new source of contrast, the dipolar relaxation time, T1, using a modified inhomogeneous magnetization transfer (ihMT) sequence. *Magn Reson Med*. 2017;78(4):1362-1372. doi:10.1002/mrm.26523
- Geeraert BL, Lebel RM, Mah AC, et al. A comparison of inhomogeneous magnetization transfer, myelin volume fraction, and diffusion tensor imaging measures in healthy children. *NeuroImage*. 2018;182:343-350. doi:10.1016/j.neuroimage.2017.09.019

- 7. Mchinda S, Varma G, Prevost VH, et al. Whole brain inhomogeneous magnetization transfer (ihMT) imaging: Sensitivity enhancement within a steady-state gradient echo sequence. *Magn Reson Med.* 2018;79(5):2607-2619. doi:10.1002/mrm.26907
- Zhang L, Chen T, Tian H, et al. Reproducibility of inhomogeneous magnetization transfer (ihMT): A test-retest, multi-site study. *Magn Reson Imaging*. 2019;57:243-249. doi:10.1016/j.mri.2018.11.010
- Lam MH, Novoselova M, Yung A, et al. Interpretation of inhomogeneous magnetization transfer in myelin water using a four-pool model with dipolar reservoirs. *Magn Reson Med*. 2025;94(1):278-292. doi:10.1002/mrm.30465
- Munsch F, Varma G, Taso M, et al. Characterization of the cortical myeloarchitecture with inhomogeneous magnetization transfer imaging (ihMT). *NeuroImage*. 2021;225:117442. doi:10.1016/j.neuroimage.2020.117442
- Alsop DC, Ercan E, Girard OM, et al. Inhomogeneous magnetization transfer imaging: Concepts and directions for further development. NMR Biomed. 2023;36(6):e4808. doi:10.1002/nbm.4808
- Hou J, Wong VW, Jiang B, et al. Macromolecular proton fraction mapping based on spinlock magnetic resonance imaging. *Magn Reson Med*. 2020;84(6):3157-3171. doi:10.1002/mrm.28362
- Gao Z, Yu Z, Zhou Z, et al. Orientation-independent quantification of macromolecular proton fraction in tissues with suppression of residual dipolar coupling. NMR Biomed. 2025;38(1):e5293. doi:10.1002/nbm.5293
- 14. Shan Q, Yu Z, Jiang B, et al. Quantitative macromolecular proton fraction imaging using pulsed spin-lock. *Magn Reson Med.* 2025. doi:10.1002/mrm.70021
- 15. Gao Z, Zhou, Z, Yu Z, et al. Orientation-Independent Magnetization Transfer Imaging of Brain White Matter. *NeuroImage*. In press.

- Malik SJ, Teixeira RPAG, West DJ, Wood TC, Hajnal JV. Steady-state imaging with inhomogeneous magnetization transfer contrast using multiband radiofrequency pulses. *Magn Reson Med.* 2020;83(3):935-949. doi:10.1002/mrm.27984
- Yarnykh VL. Fast macromolecular proton fraction mapping from a single off-resonance magnetization transfer measurement. *Magn Reson Med.* 2012;68(1):166-178. doi:10.1002/mrm.23224
- Hertanu A, Soustelle L, Le Troter A, et al. T1D-weighted ihMT imaging Part I. Isolation of long- and short-T1D components by T1D-filtering. *Magn Reson Med*. 2022;87(5):2313-2328. doi:10.1002/mrm.29139
- Hertanu A, Soustelle L, Buron J, et al. T1D-weighted ihMT imaging Part II. Investigating the long- and short-T1D components correlation with myelin content. Comparison with R1 and the macromolecular proton fraction. *Magn Reson Med*. 2022;87(5):2329-2346. doi:10.1002/mrm.29140
- Hou J, Wong VWS, Qian Y, et al. Detecting Early-Stage Liver Fibrosis Using Macromolecular Proton Fraction Mapping Based on Spin-Lock MRI: Preliminary Observations. J Magn Reson Imaging. 2023;57(2):485-492. doi:10.1002/jmri.28308
- 21. Stanisz GJ, Odrobina EE, Pun J, et al. T1, T2 relaxation and magnetization transfer in tissue at 3T. *Magn Reson Med*. 2005;54(3):507-512. doi:10.1002/mrm.20605
- Assländer J, Mao A, Marchetto E, et al. Unconstrained quantitative magnetization transfer imaging: Disentangling T1 of the free and semi-solid spin pools. *Imaging Neurosci*. 2024;2:1-16. doi:10.1162/imag\_a\_00177
- Sled JG, Pike GB. Quantitative interpretation of magnetization transfer in spoiled gradient echo MRI sequences. *J Magn Reson San Diego Calif 1997*. 2000;145(1):24-36. doi:10.1006/jmre.2000.2059
- 24. Malik SJ, Teixeira RPAG, West DJ, Wood TC, Hajnal JV. Steady-state imaging with

- inhomogeneous magnetization transfer contrast using multiband radiofrequency pulses. *Magn Reson Med.* 2020;83(3):935-949. doi:10.1002/mrm.27984
- 25. Wasserthal J, Neher P, Maier-Hein KH. TractSeg Fast and accurate white matter tract segmentation. *NeuroImage*. 2018;183:239-253. doi:10.1016/j.neuroimage.2018.07.070
- Hertanu A, Soustelle L, Buron J, et al. Inhomogeneous Magnetization Transfer (ihMT) imaging in the acute cuprizone mouse model of demyelination/remyelination.
   NeuroImage. 2023;265:119785. doi:10.1016/j.neuroimage.2022.119785
- Chen G, Fu S, Chen P, et al. Reduced myelin density in unmedicated major depressive disorder: An inhomogeneous magnetization transfer MRI study. *J Affect Disord*. 2022;300:114-120. doi:10.1016/j.jad.2021.12.111
- 28. Soustelle L, Mchinda S, Hertanu A, et al. Inhomogeneous magnetization transfer (ihMT) imaging reveals variable recovery profiles of active MS lesions according to size and localization. *Imaging Neurosci*. 2024;2:imag-2-00235. doi:10.1162/imag a 00235
- Manning AP, Chang KL, MacKay AL, Michal CA. The physical mechanism of "inhomogeneous" magnetization transfer MRI. *J Magn Reson*. 2017;274:125-136. doi:10.1016/j.jmr.2016.11.013
- Carvalho VND, Hertanu A, Grélard A, et al. MRI assessment of multiple dipolar relaxation time (T1D) components in biological tissues interpreted with a generalized inhomogeneous magnetization transfer (ihMT) model. *J Magn Reson*. 2020;311:106668. doi:10.1016/j.jmr.2019.106668
- 31. Yarnykh VL, Yuan C. Cross-relaxation imaging reveals detailed anatomy of white matter fiber tracts in the human brain. *NeuroImage*. 2004;23(1):409-424. doi:10.1016/j.neuroimage.2004.04.029
- 32. Pampel A, Müller DK, Anwander A, Marschner H, Möller HE. Orientation dependence of magnetization transfer parameters in human white matter. *NeuroImage*. 2015;114:136-

- 146. doi:10.1016/j.neuroimage.2015.03.068
- 33. Yablonskiy DA, Sukstanskii AL. Quantum dipole interactions and transient hydrogen bond orientation order in cells, cellular membranes and myelin sheath: Implications for MRI signal relaxation, anisotropy, and T1 magnetic field dependence. *Magn Reson Med*. 2024;91(6):2597-2611. doi:10.1002/mrm.29996
- 34. Morris SR, Frederick R, MacKay AL, Laule C, Michal CA. Orientation dependence of inhomogeneous magnetization transfer and dipolar order relaxation rate in phospholipid bilayers. *J Magn Reson*. 2022;338:107205. doi:10.1016/j.jmr.2022.107205
- 35. Hou J, Cai Z, Chen W, So TY. Spin-lock based fast whole-brain 3D macromolecular proton fraction mapping of relapsing–remitting multiple sclerosis. *Sci Rep.* 2024;14(1):17943. doi:10.1038/s41598-024-67445-4
- 36. Zaiss M, Zu Z, Xu J, et al. A combined analytical solution for chemical exchange saturation transfer and semi-solid magnetization transfer: AN ANALYTICAL SOLUTION FOR CEST AND MT. NMR Biomed. 2015;28(2):217-230. doi:10.1002/nbm.3237

Table 1. The mean  $\,\pm\,$  std of  $\,R_{dosl}$ ,  $T_{1D}$ -fit and  $T_{1D}$ -dic maps across major 16 fiber bundles

	Rdosl(Hz)	T1D_fit(ms)	T1D_dic(ms)
AF_left	0.2135±0.0472	4.3296±0.8916	4.5031±1.0930
AF_right	0.2107±0.0496	4.2600±0.9700	4.3862±1.1532
ATR_left	0.1978±0.0545	4.0953±1.0581	4.2079±1.2598
ATR_right	0.1910±0.0536	3.9312±1.0666	3.9843±1.2314
CC_2	0.1966±0.0536	4.1849±1.2505	4.3294±1.4197
CC_3	0.2129±0.0501	4.4934±1.3208	4.7608±1.4165
CC_5	0.2255±0.0465	4.7888±1.2762	5.1336±1.4848
CC_7	0.1951±0.0502	4.1422±1.2696	4.2707±1.2977
CG_left	0.2077±0.0442	4.3002±0.8948	4.4267±1.0795
CG_right	0.1945±0.0507	4.0314±0.9918	4.1123±1.1940
OR_left	0.1867±0.0443	3.9661±0.9538	4.0245±1.1095
OR_right	0.1910±0.0441	4.1018±1.0080	4.1751±1.1287
MLF_left	0.2069±0.0392	4.2962±0.8355	4.4433±1.0186
MLF_right	0.2135±0.0415	4.4970±0.9946	4.7022±1.1738
FPT_left	0.2262±0.0459	4.7435±0.9321	4.9899±1.1938
FPT_right	0.2139±0.0476	4.4396±0.9406	4.5826±1.1447

## Figures

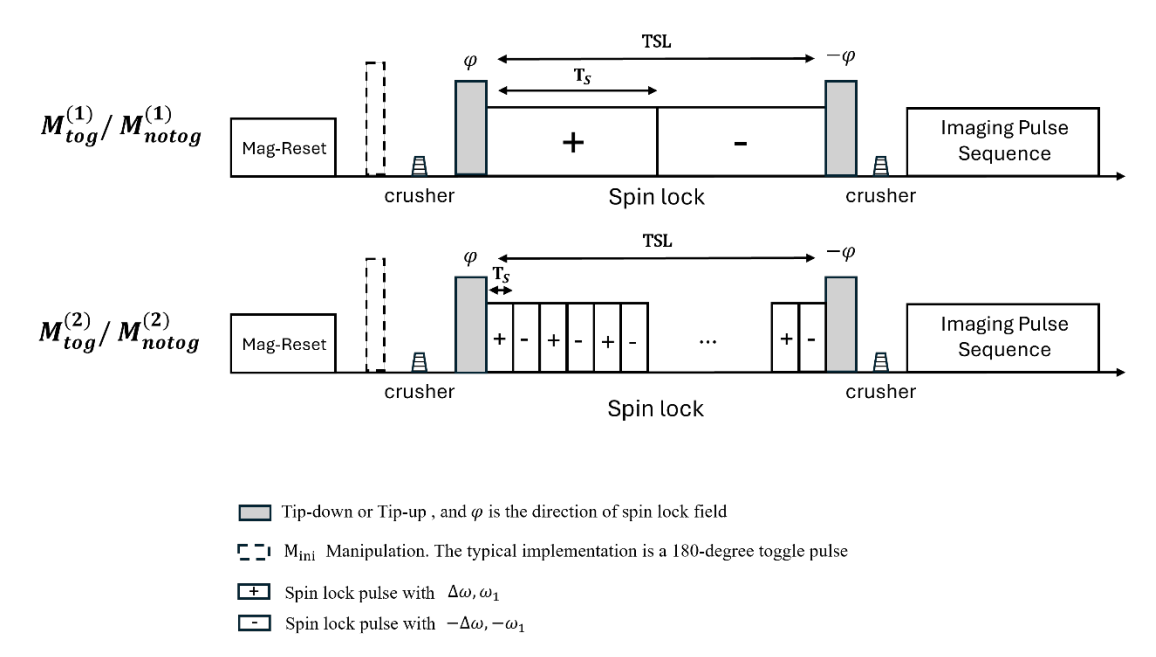


Figure 1. The illustration of single frequency and dual frequency spin-lock pulsed RF sequence.

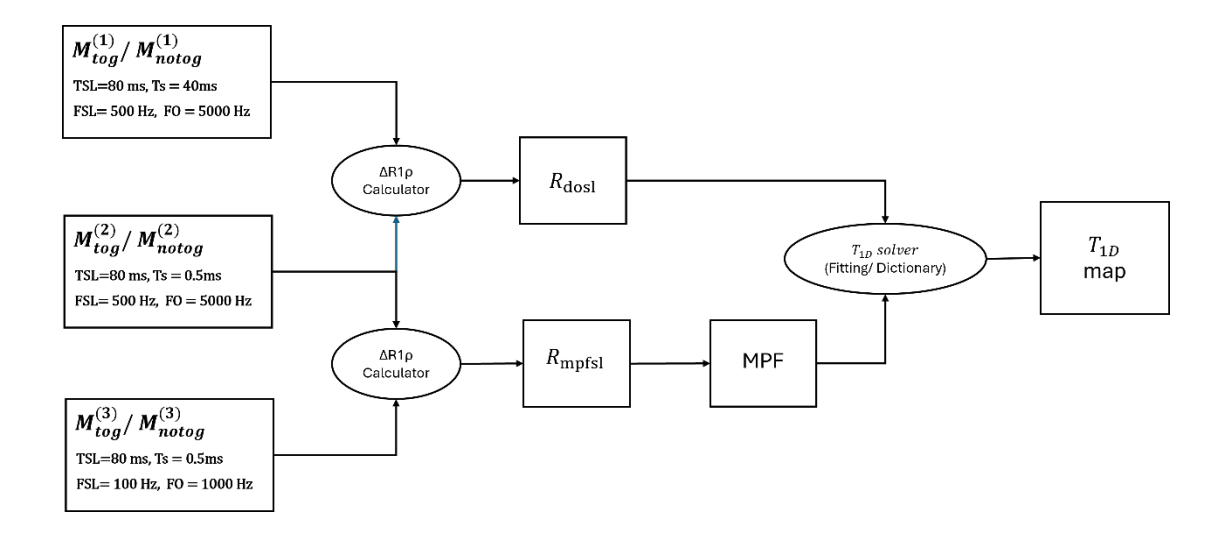


Figure 2. The workflow of acquisition scheme for white matter.

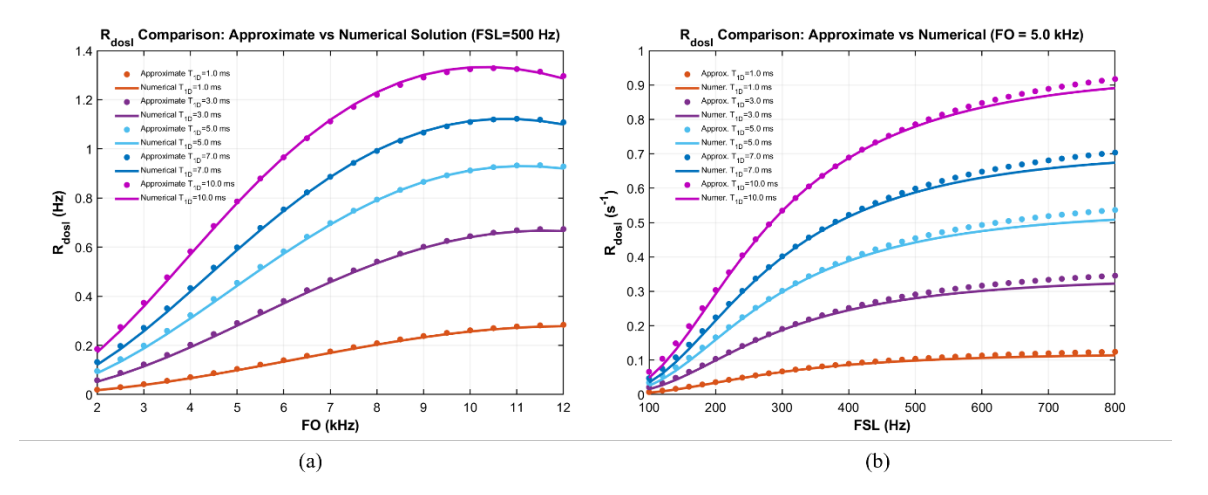


Figure 3. The comparison of approximate  $R_{dosl}$  and its Numerical solution. (a) The relationship between  $R_{dosl}$  and FO (2-12kHz) at a fixed FSL of 500 Hz. For each  $T_{1D}$  (1, 3, 5, 7, 10 ms), the approximate results (markers) closely track the numerical solution curves (solid lines). (b) The relationship between  $R_{dosl}$  and FSL (100–800 Hz) at a fixed FO of 5 kHz. The same agreement between approximate (marker) and numerical (solid lines) results is observed.

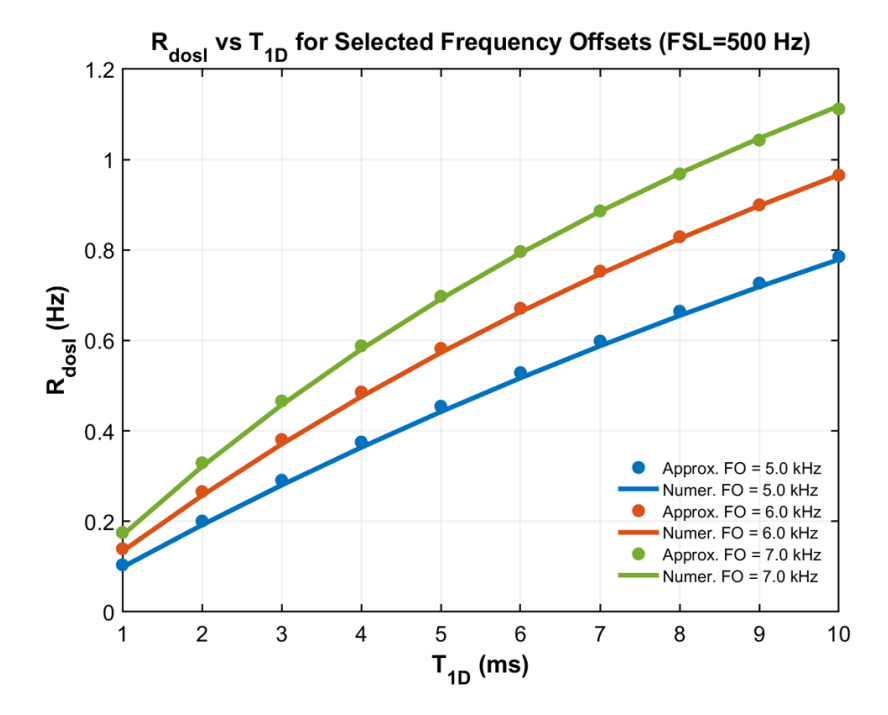


Figure. 4. The relationship between  $R_{dosl}$  and  $T_{1D}$  at fixed FSL= 500Hz with selected FO = 5,6, and 7 kHz. Approximate results (markers) closely match numerical solutions (solid lines) over T1d = 1–10 ms. For all FO values,  $R_{dosl}$  increases with  $T_{1D}$  and is nearly linear across this range, confirming the high sensitivity of  $R_{dosl}$  to  $T_{1D}$ .

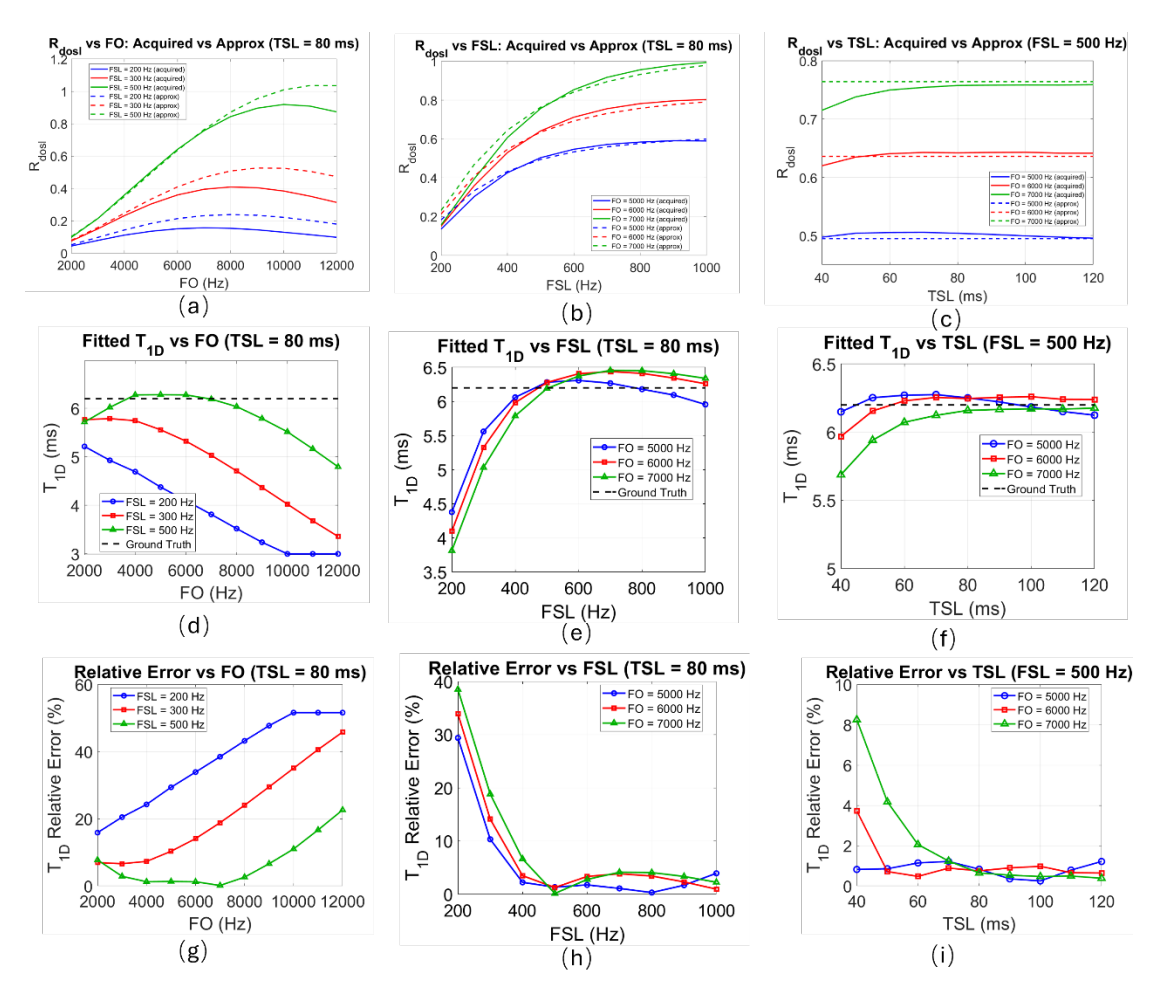


Figure 5. The simulation of comparison of acquired and approximate  $R_{dosl}$  and fitted  $T_{1D}$ . (a) The relationship between  $R_{dosl}$  and FO (2-12kHz) at fixed TSL= 80 ms and the selected FSL of 200, 300, and 500 Hz. (b) The relationship between  $R_{dosl}$  and FSL (200-1000Hz) at fixed TSL= 80 ms and the selected FO of 5000, 6000, 7000kHz. (c) The relationship between  $R_{dosl}$  and TSL (40-120ms) at fixed FSL= 500Hz and the selected FO of 5000, 6000, 7000kHz. (d)-(f) The relationship between Fitted  $T_{1D}$  and FO, FSL and TSL at corresponding selected spin-lock pulse parameter. The dot line indicates the ground truth  $T_{1D}=6.2\,\mathrm{ms}$  (g)-(i) The corresponding relative error between Fitted  $T_{1D}$  and ground truth.

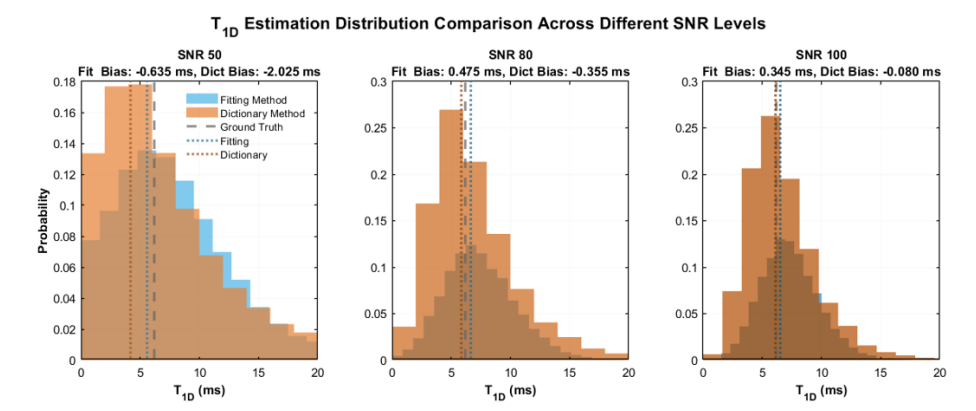


Figure 6. The distribution of  $T_{1D}$  estimation across different SNR levels. The distribution of blue color indicates the  $T_{1D}$  estimation using fitting-based  $T_{1D}$  and the distribution of orange color indicates the  $T_{1D}$  estimation using dictionary-based  $T_{1D}$ . The black dot line denotes the ground truth  $T_{1D} = 6.2 \text{ms}$ 

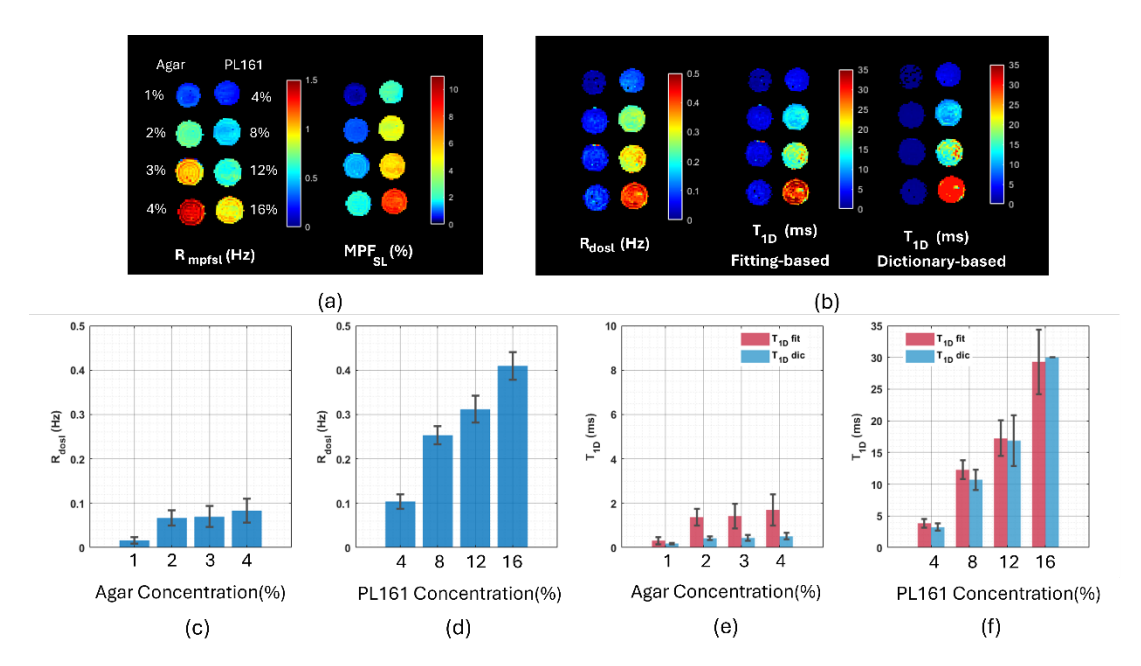


Figure 7. The results of Phantom studies. (a)  $R_{mpfsl}$  and MPF maps. (b)  $R_{dosl}$ , fitting-based  $T_{1D}$ , and dictionary-based  $T_{1D}$  map. Note the first row are agar phantom with concentration with 1%, 2%, 3%, and 4% from top to bottom, the second row are PL161 phantom with concentration 4%, 8%, 12%, and 16%, respectively. (c) and (d) the bar graph analysis for  $R_{dosl}$  to different concentration of agar phantom and PL161 phantom. (e) and (d) the corresponding bar graph analysis for  $T_{1D}$  map. The bule color indicates the dictionary-based  $T_{1D}$  map and red color for fitting-based  $T_{1D}$ .

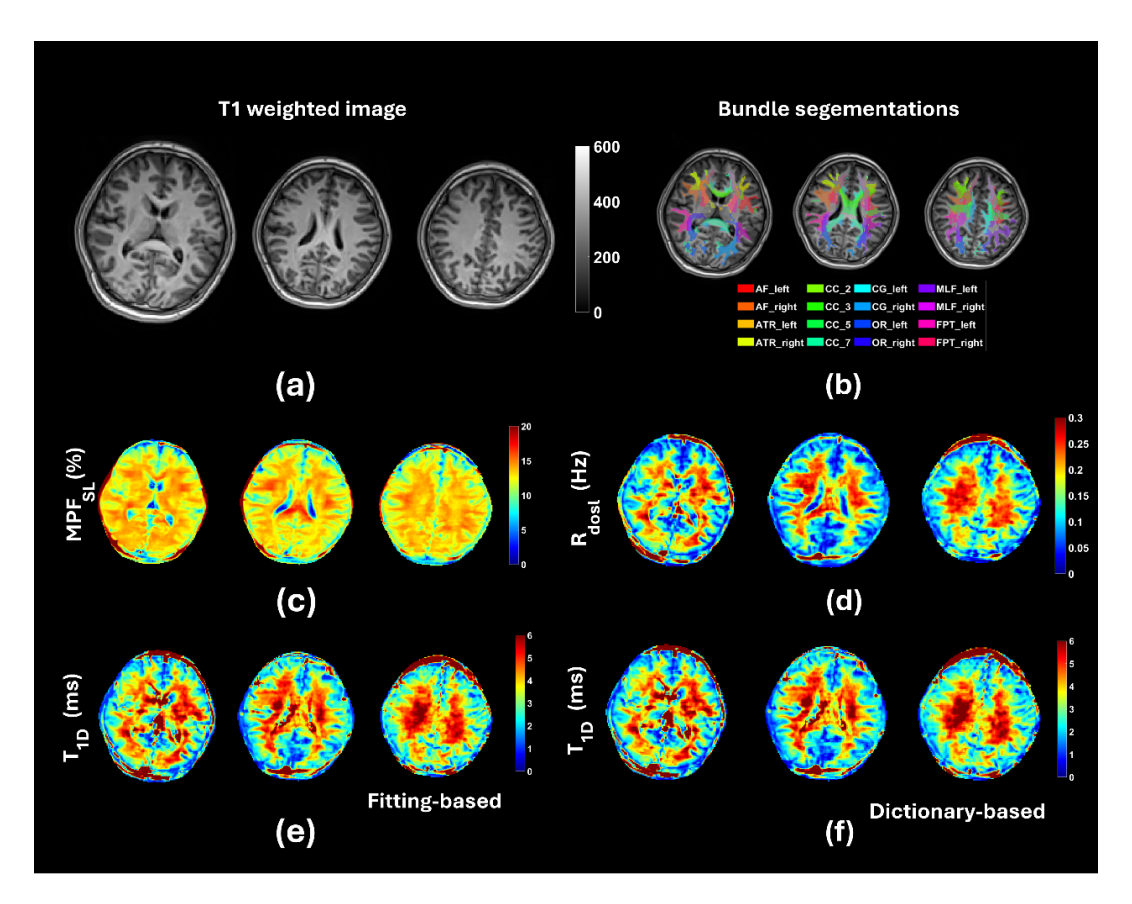


Figure 8. The results of one volunteer experiment. (a) The  $T_{1D}$  weighted image in selected slices. (b) The bundle segmentation at 16 major white matter fiber bundle. (c) The MPF maps based on MPF-SL (d)  $R_{dosl}$  maps. (e) Fitting-based  $T_{1D}$  maps. (f) Dictionary-based  $T_{1D}$  maps.

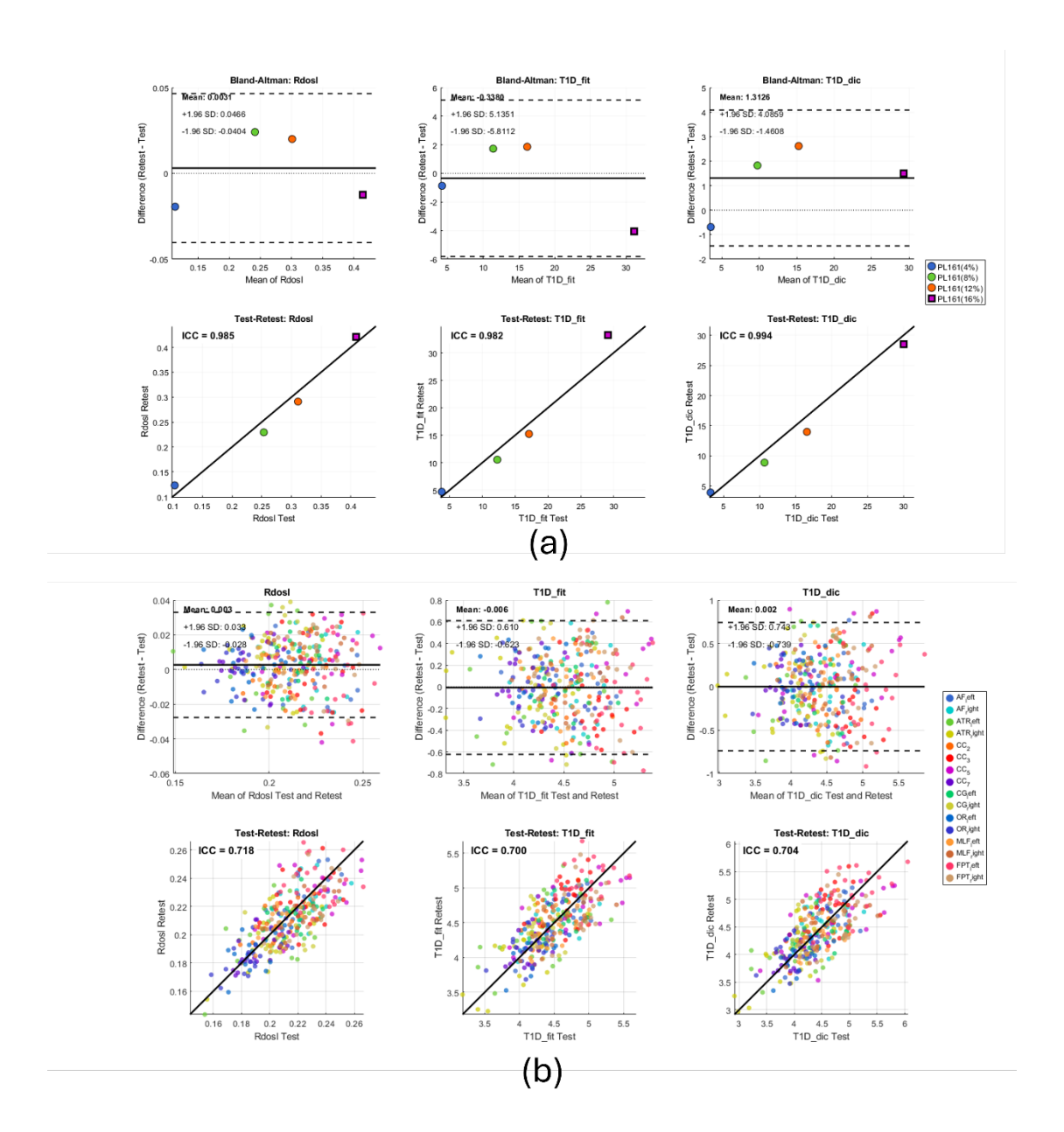


Figure 9. Test-retest reproducibility of phantom studies and in-vivo experiments. (a) The bland-Altman plots and correlation plot for PL161 phantom studies across four concentrations. (b)The bland-Altman plots and correlation plot for human studies across 16 major white matter fiber bundle in 10 volunteers.

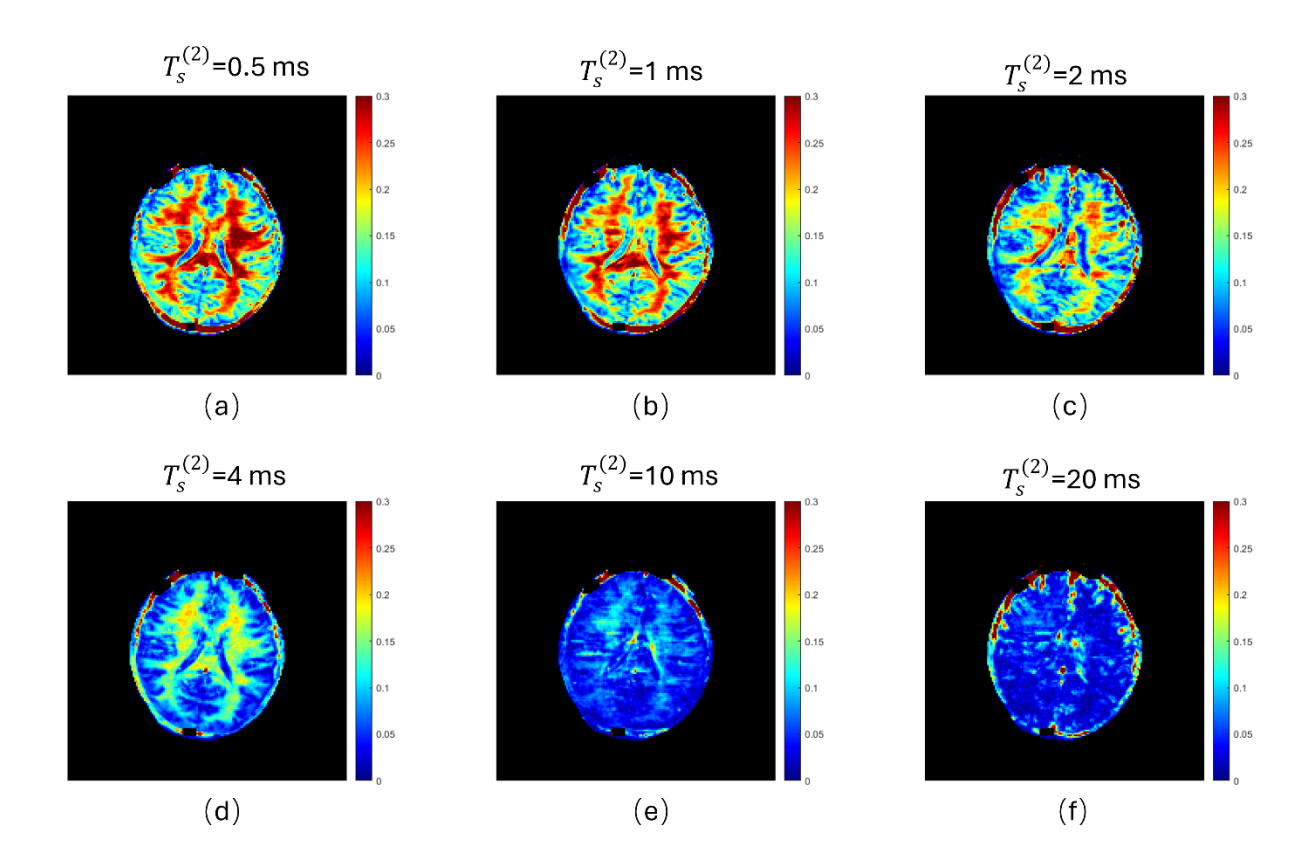


Figure S1.  $R_{dosl}$  maps across  $T_s^{(2)} = 0.5, 1, 2, 4, 10, \text{ and } 20 \text{ ms.}$